





## Quantum oscillations and anomalous angle-dependent magnetoresistance in the topological candidate $\text{Ag}_3\text{Sn}$

Nan Zhou <sup>1,2,\*</sup> Yue Sun <sup>4,†</sup> C. Q. Xu,<sup>1</sup> C. Y. Xi,<sup>3</sup> Z. S. Wang,<sup>3</sup> B. Li <sup>6</sup>, J. J. Feng,<sup>1</sup> L. Zhang,<sup>3</sup> X. Z. Xing,<sup>1</sup> Y. F. Zhang <sup>1</sup>, Y. Q. Pan,<sup>1</sup> Y. Meng,<sup>1</sup> X. L. Yi,<sup>1</sup> L. Pi,<sup>3</sup> Xiaofeng Xu,<sup>5</sup> and Zhixiang Shi<sup>1,‡</sup>

<sup>1</sup>*School of Physics and Key Laboratory of MEMS of the Ministry of Education, Southeast University, Nanjing 211189, China*

<sup>2</sup>*Institute for Solid State Physics (ISSP), The University of Tokyo, Kashiwa, Chiba 277-8581, Japan*

<sup>3</sup>*Anhui Province Key Laboratory of Condensed Matter Physics at Extreme Conditions, High Magnetic Field Laboratory, Chinese Academy of Sciences, Hefei 230031, China*

<sup>4</sup>*Department of Physics and Mathematics, Aoyama Gakuin University, Kanagawa 252-5258, Japan*

<sup>5</sup>*Department of Applied Physics, Zhejiang University of Technology, Hangzhou 310023, China*

<sup>6</sup>*New Energy Technology Engineering Laboratory of Jiangsu Province and School of Science, Nanjing University of Posts and Telecommunications, Nanjing 210023, China*



(Received 4 July 2019; accepted 11 May 2020; published 1 June 2020)

Because of their unique electronic structure and peculiar physical properties, topological materials have attracted considerable attention in condensed matter physics. In both physics and material science, exploring materials with a topological state or Dirac fermions near the Fermi level is important. Here, we report the transport evidence of the topological state for  $\text{Ag}_3\text{Sn}$ . Under a high magnetic field, we observed clear Shubnikov–de Haas (SdH) oscillations with three major frequencies and relatively small effective masses. Our SdH quantum oscillation analyses reveal that the Berry phase of the  $\gamma$  band is very close to the nontrivial value  $\pi$ ; the nonzero Berry phase for the  $\alpha$  band indicates the  $\text{Ag}_3\text{Sn}$  alloy to be a possible topological material. Moreover, we performed angle-resolved magnetoresistance (MR) measurements. Note that MR displays an unusual angular dependence, which can be tuned from twofold to fourfold symmetry by temperature and field. This feature makes  $\text{Ag}_3\text{Sn}$  a candidate for valleytronics.

DOI: [10.1103/PhysRevB.101.245102](https://doi.org/10.1103/PhysRevB.101.245102)

### I. INTRODUCTION

Identifying materials with topological anomalies in their electronic structure is of great important in condensed matter physics [1–9] because of the fascinating physics of the fundamental studies and the potential for device-based applications. Some materials not only host topological states but also exhibit large magnetoresistance (MR) [2,5,10], high carrier mobility [2,5,10], and quantum oscillations with a nontrivial  $\pi$  Berry phase [3,5–7,9,11,12], which come from the corresponding fermions hosted by Dirac or Weyl cones. Furthermore, only a few of these materials manifest a multivalley effect [3,8], revealing that the electric conductivity is the sum of the contributions of different valleys. Each valley is extremely sensitive to the orientation and magnitude of the magnetic field [13]. Both of a high [14] or a rotating [13] magnetic field could remove valleys and observe a valley-emptying. These topological materials with the abundant physical properties have attracted considerable attention. Recently, the large MR was discovered in  $\text{ASn}_4$  ( $A = \text{Pt}, \text{Rh}, \text{and Pd}$ ) [3,4,15–17], of which both  $\text{PtSn}_4$  [4,15] and  $\text{PdSn}_4$  [3,16] exhibit topological properties and a clear oscillation. These peculiar results suggest that the pertinent stannide systems will show interesting physics.

Similar to  $\text{ASn}_4$ , topological state was predicted in  $\text{Ag}_3\text{Sn}$  [18,19]. Although  $\text{Ag}_3\text{Sn}$  was discovered in 1926 [20], its crystal structure is still under debate [21,22]. Previous x-ray diffraction (XRD) studies by Nial [23] on powder specimens and a recent study on nanoparticle materials [22] suggested that  $\text{Ag}_3\text{Sn}$  exhibits the orthorhombic structure of  $Cmcm$ . Another recent study reported that  $\text{Ag}_3\text{Sn}$  undergoes polymorphic phase transformations with the hexagonal  $P63/mmc$  structure at a high temperature and the orthorhombic  $Cmcm$  structure at a low temperature [24]. However, an orthorhombic structure with the space group of  $Pmnm$  [25,26] was confirmed using transmission electron microscopy [26] between 253 and 453 K. The complex structure of  $\text{Ag}_3\text{Sn}$  makes the study of its physical properties challenging.

In this study, we systematically investigated the transport properties of a pure, monocrystalline  $\text{Ag}_3\text{Sn}$  with the space group of  $Pmnm$ ; its large linear MR and unexpected quantum oscillations indicate  $\text{Ag}_3\text{Sn}$  to be a possible topological material with a nontrivial Berry phase. Moreover,  $\text{Ag}_3\text{Sn}$  displays an unusual polar angle-resolved magnetoresistance (AMR) with tunable symmetry from twofold to fourfold by temperature and field, making it a candidate for valleytronics.

### II. EXPERIMENT

$\text{Ag}_3\text{Sn}$  single crystals were grown using a self-flux method. Silver (Ag, 99.99%) and tin (Sn, 99.99%) powders were mixed thoroughly in the ratio of 1:20, after which the blended

\*Corresponding author: 230159455@seu.edu.cn

†Corresponding author: sunyue@phys.aoyama.ac.jp

‡Corresponding author: zxshi@seu.edu.cn

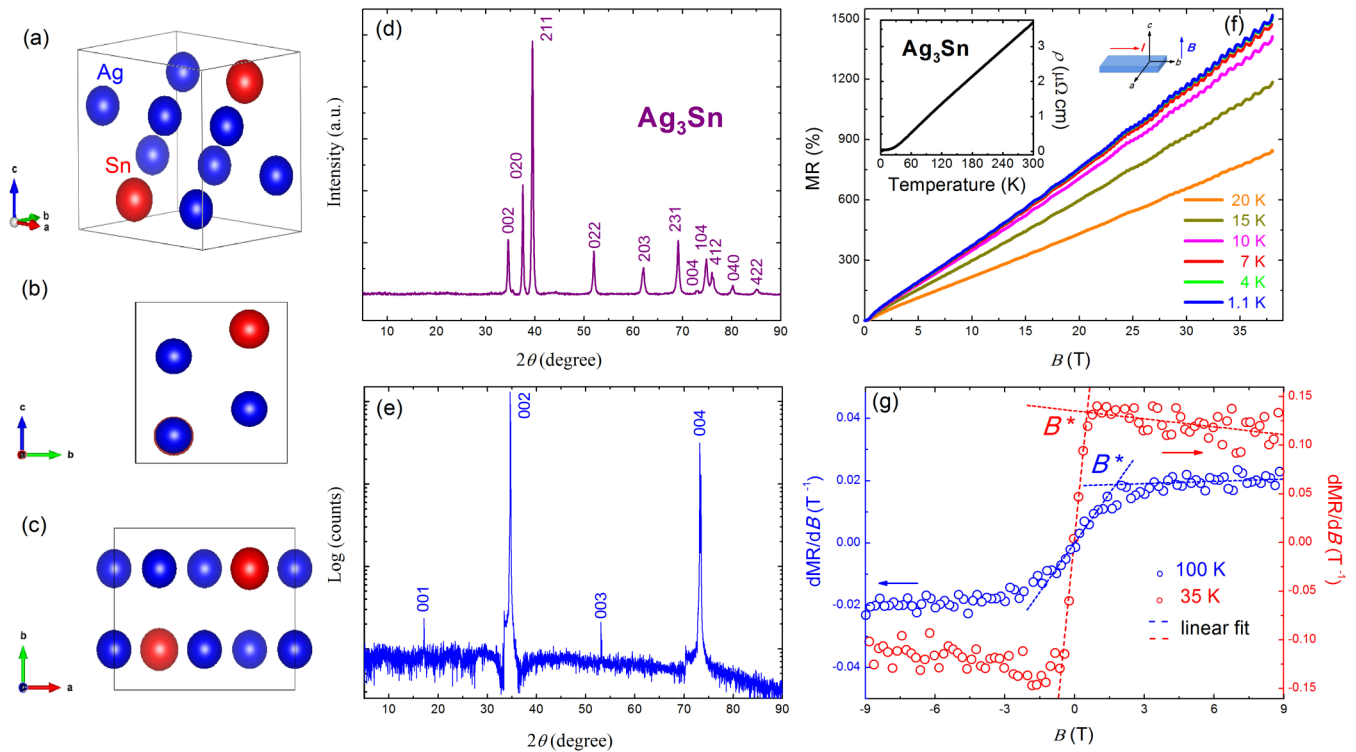


FIG. 1. (a) The crystallographic structure of  $\text{Ag}_3\text{Sn}$  with an orthorhombic unit cell, (b) atomic configuration in the (100) plane, (c) atomic configuration in the (001) plane. (d) The powder XRD pattern of  $\text{Ag}_3\text{Sn}$ , (e) single-crystal XRD pattern, (f) SdH oscillations of MR at various temperatures (inset shows the configuration of the measurement and the temperature dependence of the electrical resistivity at 0 T), and (g) magnetic field ( $B$ ) derivatives of MR at 35 and 100 K. The data were fitting using  $\text{MR} = A_2 B^2$  at a low magnetic field, while using  $\text{MR} = A_1 B + O(B^2)$  at a high magnetic field.

powder sample was loaded into and sealed in an evacuated quartz tube; the tube was heated to 543 K and maintained at that temperature for 3 days. Subsequently, it was slowly cooled to 473 K and directly quenched in iced water. An ingot composed of Ag and excess Sn was obtained and dissolved using dilute hydrochloric acid. After this process, a large number of plate-like single crystals could be harvested. The structure of  $\text{Ag}_3\text{Sn}$  was characterized by XRD with  $\text{Cu } K_\alpha$  radiation. The directions of the crystal axes were determined by single-crystal XRD. In particular, the temperature evolution of the single-crystal XRD patterns was measured. The crystal composition was determined by energy-dispersive x-ray spectroscopy (EDX). We measured the resistivity, AMR, and the Hall effect using a physical property measurement system (PPMS, Quantum Design). The high field transport measurements of the  $\rho_{yy}$  were carried out using standard ac lock-in techniques with a  $^3\text{He}$  cryostat and a dc-resistive magnet ( $\sim 38$  T) at the High Magnetic Field Laboratory of Chinese Academy of Sciences. While, the measurements of the  $\rho_{xx}$  and  $\rho_{xy}$  were performed in the Institute for Solid State Physics (ISSP), the University of Tokyo, Japan by using the pulse magnetic field ( $\sim 42$  T). We performed magnetization measurements using a superconducting quantum interference device (SQUID) magnetometer (MPMS-7, Quantum Design).

### III. RESULTS AND DISCUSSION

Figures 1(a)–1(c) show the crystallographic structure of  $\text{Ag}_3\text{Sn}$ ; each unit cell has six Ag atoms and two Sn atoms

[27]. The average atomic ratio is determined to be Ag:Sn = 3:1 by EDX. Note that the powder XRD patterns [Fig. 1(d)] are consistent with previous results [28] and can be indexed to the space group of  $Pm\bar{m}n$  with an orthorhombic unit cell of  $a = 5.963$  Å,  $b = 4.786$  Å, and  $c = 5.187$  Å. The single-crystal XRD pattern only contains the (00 $l$ ) peaks [Fig. 1(e)], indicating that the  $c$  axis is perfectly perpendicular to the plane of the single crystals.

The inset of Fig. 1(f) shows the zero-field temperature-dependent resistivity of  $\text{Ag}_3\text{Sn}$ .  $\text{Ag}_3\text{Sn}$  demonstrates an extremely small resistivity ( $\sim 0.04$   $\mu\Omega$  cm at 2.5 K). The resistivity maintains almost linear  $T$  dependence and quickly increased with increase in magnetic field [Fig. 1(f)], corresponding to a large, nonsaturating linear MR that reach 1500% under 38 T at 1.1 K. Furthermore, clear Shubnikov-de Haas (SdH) oscillations are observed. The quantum oscillations will be discussed in detail later.

The MR is different at high and low temperatures (Fig. S1 in Ref. [29]). At low temperatures, the MR exhibits a quasilinear behavior; however, at the high temperatures, a significant deviation from the linear behavior is observed. The nonsaturating quasilinear MR may be related to a scenario in which the Dirac point is near the Fermi surface [17,30]. The linear MR can be seen more clearly by plotting the first-order derivative of the MR ( $d(\text{MR})/dB$ ) [Fig. 1(g)]. For a low magnetic field,  $d(\text{MR})/dB$  is proportional to  $B$  and MR exhibits a semiclassical quadratic field dependence. However, the slope of  $d(\text{MR})/dB$  abruptly reduces to nearly 0 at a high magnetic field, which could be explained by quantum

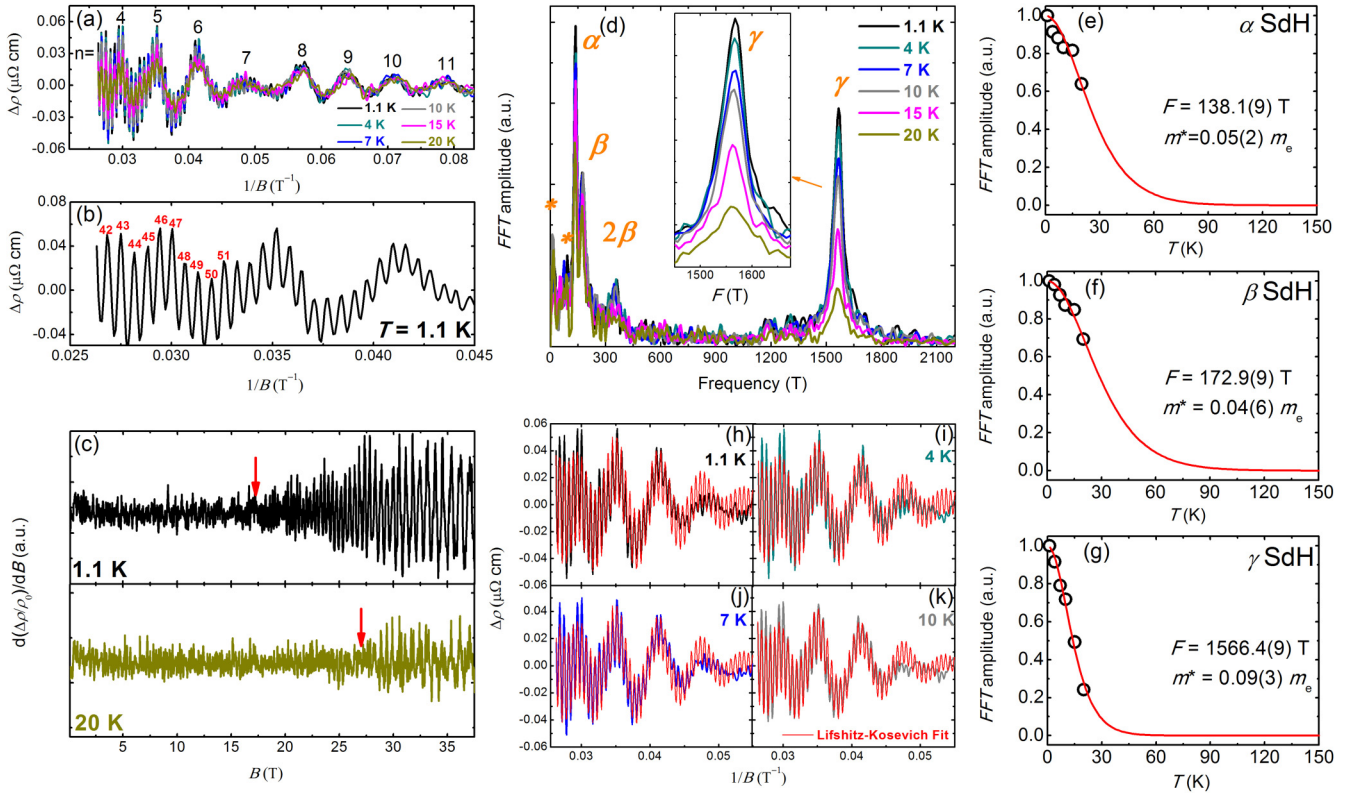


FIG. 2. (a) The oscillatory component of the resistivity  $\Delta\rho$ , extracted from  $\rho$  by subtracting a smoothed polynomial background, as a function of  $B^{-1}$  at several temperatures, (b) oscillatory component of the resistivity  $\Delta\rho$  at 1.1 K. (c)  $d(\Delta\rho/\rho_0)/dB$  as a function of magnetic field at  $T = 1.1$  and 20 K. (d) FFT of the corresponding SdH oscillations in  $\text{Ag}_3\text{Sn}$  plotted as a function of temperature. The insets show magnified  $\gamma$  band data, and [(e)–(g)] normalized amplitude of the FFT of the SdH oscillations in  $\text{Ag}_3\text{Sn}$  plotted as a function of temperature. The effective masses of the carriers can be extracted from the Lifshitz–Kosevich (LK) fit. [(h)–(k)] Fits of the oscillation patterns to the multiband LK formula at  $T = 1.1, 4, 7,$  and 10 K, respectively.

linear transport plus a very small semiclassical quadratic term.

To learn more about the electronic states, we investigated the SdH oscillations, which has proven to be effective for studying topological-nontrivial transport [8,12,31]. Using the data in Fig. 1(f),  $d(\Delta\rho/\rho_0)/dB$  is plotted as a function of magnetic field [Fig. 2(c)]. At 1.1 K, quantum oscillations are discernible around  $B = 17$  T; at 20 K, the onset of oscillation occurs at a significantly higher magnetic field, up to 27 T. After subtracting a smoothed polynomial background, the residual signals of  $\Delta\rho$  show an obvious periodic behavior and become more apparent at a low temperature [Fig. 2(a)]; moreover, an additional high-frequency mode is detected under a high magnetic field [Fig. 2(b)], indicating that there is more than one principle oscillation frequency in  $\text{Ag}_3\text{Sn}$ .

To confirm the oscillation frequencies and obtain more information about the Fermi surface, we implemented a fast fourier transform (FFT) on data taken at various temperatures [Fig. 2(d)]. Our FFT analyses of  $\Delta\rho$  reveals multiple frequencies, including three sets of major frequencies,  $\alpha$  (138.19 T),  $\beta$  (172.99 T), and  $\gamma$  (1566.49 T), as well as the additional peak  $2\beta$  (345 T) corresponding to the second harmonic of major frequency  $\beta$ . According to the Onsager relation  $F = (\phi_0/2\pi^2)A = (\hbar/2\pi e)A$ , frequency  $F$  is proportional to  $A$ , and  $A$  denotes the cross section of the Fermi surface normal to the magnetic field. Considering a circular cross section, we obtain

the Fermi surface area  $A$  for  $\alpha$ ,  $\beta$ , and  $\gamma$ , as summarized in Table I.

For a multifrequency system, the amplitude of the SdH oscillation can be described by the LK formula [32,33]

$$\frac{\Delta\rho}{\rho_0} = \frac{5}{2} \left( \frac{B}{2F} \right)^{1/2} \frac{2\pi^2 k_B T m^* / eB\hbar}{\sinh(2\pi^2 k_B T m^* / eB\hbar)} e^{-2\pi^2 k_B T_D m^* / eB\hbar} \times \cos \left[ 2\pi \left( \frac{F}{B} + \frac{1}{2} - \frac{\phi_B}{2\pi} + \delta \right) \right], \quad (1)$$

where  $m^*$  is the effective mass of the carrier,  $T_D$  is the Dingle temperature, and  $\phi_B$  is the Berry phase. The phase shift  $\delta$  is determined by the dimensionality of the Fermi surface with the value of  $\delta = 0$  (or  $\pm 1/8$ ) for a two-dimensional [or three-dimensional (3D)] system. In Eq. (1), the thermal damping term  $\frac{2\pi^2 k_B T m^* / eB\hbar}{\sinh(2\pi^2 k_B T m^* / eB\hbar)}$  can be used to independently extract the effective mass  $m^*$ , as shown in Figs. 2(e)–2(g). The obtained effective masses  $m^*$  for all the frequencies are focused in the range of 0.045–0.1 $m_e$  (Table I); they are comparable with that of  $\text{Cd}_3\text{As}_2$  [11] and  $\text{YbMnSb}_2$  [6]. The relatively small effective mass is a characteristic of Dirac fermions [6].

The Berry phase  $\phi_B$  can be obtained by mapping the Landau level (LL) index fan diagrams based on the Lifshitz–Onsager quantization rule. The comparison between the  $\rho_{xx}\rho_{yy}$  and  $\rho_{xy}^2$  is important for assigning the LL index. When

TABLE I. Parameters derived from the SdH oscillations at 1.1 K.  $F$ , oscillation frequency;  $A$ , cross-sectional area of Fermi surface;  $k_F$ , Fermi vector, assuming a circular cross-section;  $T_D$ , Dingle temperature;  $m^*$ , effective mass;  $\tau_q$ , quantum lifetime;  $\mu_q$ , quantum mobility;  $v_F$ , Fermi velocity;  $E_F$ , Fermi energy; and  $\phi_B$ , Berry phase.

	$F$ (T)	$A$ (Å <sup>-2</sup> )	$k_F$ (Å <sup>-1</sup> )	$T_D$ (K)	$m^*/m_e$	$\tau_q$ (10 <sup>-14</sup> s)	$\mu_q$ (cm <sup>2</sup> V <sup>-1</sup> s <sup>-1</sup> )	$v_F$ (10 <sup>6</sup> m/s)	$E_F$ (eV)	$\phi_B$ (LK fits, $\delta = \pm \frac{1}{8}$ )
$\alpha$	138.1(9)	0.01(3)	0.06(5)	104.2(3)	0.05(2)	1.1(7)	394.4(8)	1.4(5)	0.6(2)	$[0.35(9) \pm 0.25]\pi$
$\beta$	172.9(9)	0.01(6)	0.07(1)	109.1(4)	0.04(6)	1.1(1)	425.8(8)	1.7(9)	0.8(4)	$[1.34(1) \pm 0.25]\pi$
$\gamma$	1566.4(9)	0.14(9)	0.21(8)	26.0(8)	0.09(3)	4.6(6)	881.4(4)	2.7(1)	3.8(9)	$[1.12(4) \pm 0.25]\pi$

$\rho_{xx}\rho_{yy} \gg \rho_{xy}^2$ , the conductivity  $\sigma_{xx}$  oscillations are out-of-phase with the resistivity  $\rho_{xx}$ ; for the case of  $\rho_{xx}\rho_{yy} \ll \rho_{xy}^2$ , the conductivity  $\sigma_{xx}$  are almost in-phase with the resistivity  $\rho_{xx}$ . In the multifrequency Ag<sub>3</sub>Sn system, although  $\rho_{xx}\rho_{yy}$  is always larger than  $\rho_{xy}^2$ , the oscillatory components of the  $\rho_{xy}^2$  cannot be ignored (see Fig. S7(h) [29]). The comparable resistivity components could result in a complex situation in Ag<sub>3</sub>Sn system. In this case, a comprehensive analysis of the resistivity ( $\rho_{xx}$ ,  $\rho_{yy}$ ) and Hall resistivity ( $\rho_{xy}$ ) is more reliable for determining the Berry phase [33].

$$\begin{aligned} \sigma_{xx}(B) &= \sigma_{xx}^0(B) + \Delta\sigma_{xx}(B) \\ &= \sigma_{xx}^0(B) \left( 1 + \frac{\tilde{D}(B)}{D_0} \right) = \frac{\rho_{yy}}{\rho_{xx}\rho_{yy} + \rho_{xy}^2}, \end{aligned} \quad (2)$$

where  $\Delta\sigma_{xx}(B)$  is the oscillatory part of the diagonal conductivity,  $\sigma_{xx}^0(B)$  is the nonoscillatory part, and  $\tilde{D}(B)$  is the oscillatory part of density of state (DOS). The quantum oscillation of the diagonal conductivity arises from the DOS. To guarantee the reliability of the obtained Berry phase, we measure the resistivity  $\rho_{xx}$ ,  $\rho_{yy}$  and Hall resistivity  $\rho_{xy}$  [34] (see Figs. S7(a)–S7(g) [29]). The conductivity  $\sigma_{xx}$  could be obtained by using the expression of the  $\sigma_{xx} = \frac{\rho_{yy}}{\rho_{xx}\rho_{yy} + \rho_{xy}^2}$ . After subtracting a smoothed polynomial background, we implemented a FFT for the oscillatory part  $\Delta\sigma_{xx}$  (see Fig. S7(j) [29]). However, unlike the FFT spectrum in the  $\rho_{xx}$  (Fig. S7(g) [29]) and  $\rho_{yy}$  (Fig. S7(e) [29]), we cannot distinguish the peaks at 138.19 and 1566.49 T (Fig. S7(j) [29]) due to the strong noise level introduced by  $\rho_{xy}$ . We think the much smaller resistance of the  $R_{xx}$  and  $R_{yy}$  could be a primary reason, which could make the noise level becomes relatively stronger; another possible origin of the noise is the low frequency noise in the pulse high field. Future efforts on the precise measurements of  $\rho_{xx}$  and  $\rho_{xy}$  are needed to map the LL index fan diagrams.

We also directly use the LK formula (1) to fit the multifrequency SdH oscillations [Figs. 2(h)–2(k)]. The fitting yields some important parameters, as summarized in Table I and Table SI [29]. The phase shift  $\frac{1}{2} - \frac{\phi_B}{2\pi} + \delta$  from the LK fit yields Berry phases  $\phi_B$  of  $0.35(9)\pi$ ,  $1.34(1)\pi$ , and  $1.12(4)\pi$  for the three major bands of  $\alpha$ ,  $\beta$ , and  $\gamma$ , respectively. Considering the 3D Fermi surface with  $\delta = \pm 1/8$  (Fig. S2 [29]), the Berry phase of the  $\gamma$  band is very close to the nontrivial value  $\pi$ . Furthermore, a nonzero Berry phase of the  $\alpha$  band may be associated with a topological characteristic [18, 19, 35]. Certainly, there still some inevitable problems in our LK fitting. Because of the comparable resistivity components in Ag<sub>3</sub>Sn system, we could not apply the LK formula by only considering the  $\rho_{xx}$  or  $\rho_{yy}$ . Therefore future efforts on a comprehensive analysis of the resistivity ( $\rho_{xx}$ ,  $\rho_{yy}$ ) and Hall

resistivity ( $\rho_{xy}$ ) could be a more reliable way to confirm the Berry phase.

The AMR of Ag<sub>3</sub>Sn is also investigated with the relative space position relations shown schematically in Figs. 3(a) and 3(b). When the magnet field  $B$  is always perpendicular to the excitation current flow in Fig. 3(a), the AMR data exhibit a twofold symmetry at 100 K under a field of 9 T [Fig. 3(c)]. With decreasing temperature, the curve gradually evolves to a butterfly-pattern with four- or eightfold symmetry [Figs. 3(d)–3(g)]. Moreover, the symmetry of the AMR can be also tuned by the field. In Figs. 3(o) and 3(p), the twofold symmetric curve measured at 30 K is changed to fourfold symmetry by increasing the magnetic field from 2 to 8 T. To better understand the evolution of the symmetry, data was fitted by a simple trigonometric equation  $\rho(\theta) = \rho_{2\theta} + \rho_{4\theta} + \rho_{8\theta} + C$  [8]. The fitting detail is elucidated in Fig. S6 [29]. Weight of the different symmetric components are extracted shown in Figs. 3(q)–3(s). As the temperature decreases,  $A_{2\theta}$  is gradually suppressed and become very weak (or even absent). However,  $A_{4\theta}$  and  $A_{8\theta}$  are significantly enhanced and become dominant at a very low temperature. At 30 K, the symmetry corresponds to a mixed state with a dominant twofold symmetry at low magnetic field; however, it is fourfold and eightfold under a high magnetic field. Therefore the symmetry of the AMR of Ag<sub>3</sub>Sn can be simply tuned by the temperature and field. These features are similar to multivalley system of bulk bismuth [13] that strongly depends on the orientation of the magnetic field, thus indicating Ag<sub>3</sub>Sn to be a possible candidate for valleytronics. By contrast, AMR keeps a twofold symmetry in the whole temperature range when the magnet field rotates in the  $bc$  plane. Interestingly, with decreasing temperature, the twofold AMR becomes stronger and more anisotropic at low temperatures [see Figs. 3(h)–3(l)].

A natural question is related to the microscopic origin of the changing symmetry in the AMR. The crystal shows no structural transition as proven by the XRD measurements taken at different temperatures in Fig. S3 [29], which excludes the possibility of structure transition induced change in the AMR. Furthermore, we observe that both the susceptibility  $\chi$  and Hall coefficient  $R_H$  exhibit an increase below a characteristic temperature  $\sim 100$  K (Figs. S5(a) and S5(e) [29]). Meanwhile, we noticed that the onset temperature of the change in the AMR symmetry is almost identical to the characteristic temperature of  $T_\chi$  and  $T_{\text{hall}}$  (Fig. S4 of Ref. [29]). Therefore we discuss the possible scenarios of magnetic origin [36–39] in Fig. S5 [29]. Another possible origin is the Fermi surface change by the Lifshitz transition, which should be strongly anisotropic because the difference of the AMR in the  $ac$  and  $bc$  plane. Future efforts on the temperature dependence of the band structure are hopefully to solve this issue.

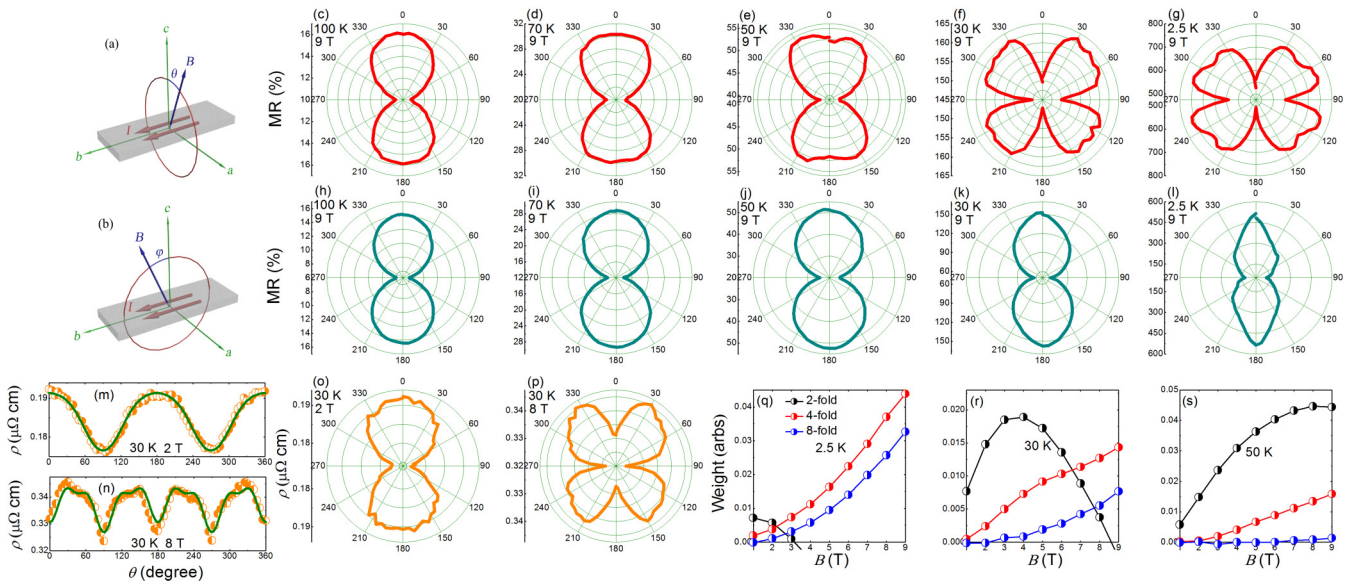


FIG. 3. [(a) and (b)] Schematic of the experimental configuration for AMR in the  $ac$  and  $bc$  planes, respectively. [(c)–(g)] Polar plots illustrating the butterfly AMR effect in the  $ac$  plane under 9 T at several temperatures. [(h)–(l)] Polar plots illustrating the twofold AMR effect in the  $bc$  plane under 9 T at several temperatures. [(m) and (n)] The fit to the AMR data at 30 K by using  $\rho(\theta) = \rho_{2\theta} + \rho_{4\theta} + \rho_{8\theta} + C$  under 2 and 8 T, respectively. [(o) and (p)] Polar plots of the AMR at  $T = 30$  K under 2 and 8 T, respectively. [(q)–(s)] The fit extracts the weighting of the twofold, fourfold, and eightfold symmetry components of the AMR between 1 and 9 T, at 2.5, 30, and 50 K, respectively.

#### IV. CONCLUSIONS

In summary, we observed clear SdH oscillations in  $\text{Ag}_3\text{Sn}$  under high magnetic fields and at low temperatures. The SdH quantum oscillation data revealed three major frequencies and relatively small effective masses. Our LK fitting reveals that the Berry phase in the  $\gamma$  band was very close to the nontrivial value  $\pi$ , and the nonzero Berry phase for the  $\alpha$  band was correlated to the topological characteristics. Besides, an unambiguous AMR deformation which can be tuned from twofold to fourfold symmetry by temperature and field, suggests the  $\text{Ag}_3\text{Sn}$  to be a candidate for valleytronics.

#### ACKNOWLEDGMENTS

The authors would like to thank Tsuyoshi Tamegai and Peng Zhang for stimulating discussions and Masashi Tokunaga and Toshiro Sakakibara for collaborative support. This work was partly supported by the National Natural Science Foundation of China (Grants No. 11674054, No. 11974061, No. U1932217, and No. U1732162), the Strategic Priority Research Program of Chinese Academy of Sciences, Grant No. XDB25000000, and JSPS KAKENHI (No. JP20H05164 and No. JP19K14661).

- [1] Z. Liu, J. Jiang, B. Zhou, Z. Wang, Y. Zhang, H. Weng, D. Prabhakaran, S. Mo, H. Peng, P. Dudin *et al.*, *Nat. Mater.* **13**, 677 (2014).
- [2] C. Shekhar, A. K. Nayak, Y. Sun, M. Schmidt, M. Nicklas, I. Leermakers, U. Zeitler, Y. Skourski, J. Wosnitza, Z. Liu *et al.*, *Nat. Phys.* **11**, 645 (2015).
- [3] C. Q. Xu, W. Zhou, R. Sankar, X. Z. Xing, Z. X. Shi, Z. D. Han, B. Qian, J. H. Wang, Z. Zhu, J. L. Zhang, A. F. Bangura, N. E. Hussey, and X. Xu, *Phys. Rev. Mater.* **1**, 064201 (2017).
- [4] Y. Wu, L.-L. Wang, E. Mun, D. D. Johnson, D. Mou, L. Huang, Y. Lee, S. L. Bud'ko, P. C. Canfield, and A. Kaminski, *Nat. Phys.* **12**, 667 (2016).
- [5] J. Hu, J. Liu, D. Graf, S. Radmanesh, D. Adams, A. Chuang, Y. Wang, I. Chiorescu, J. Wei, L. Spinu *et al.*, *Sci. Rep.* **6**, 18674 (2016).
- [6] Y.-Y. Wang, S. Xu, L.-L. Sun, and T.-L. Xia, *Phys. Rev. Mater.* **2**, 021201(R) (2018).
- [7] J. Hu, Y. L. Zhu, D. Graf, Z. J. Tang, J. Y. Liu, and Z. Q. Mao, *Phys. Rev. B* **95**, 205134 (2017).
- [8] M. N. Ali, L. M. Schoop, C. Garg, J. M. Lippmann, E. Lara, B. Lotsch, and S. S. Parkin, *Sci. Adv.* **2**, e1601742 (2016).
- [9] Y. Y. Lv, B. B. Zhang, X. Li, K. W. Zhang, X. B. Li, S. H. Yao, Y. B. Chen, J. Zhou, S. T. Zhang, M. H. Lu, S. C. Li, and Y. F. Chen, *Phys. Rev. B* **97**, 115137 (2018).
- [10] T. Liang, Q. Gibson, M. N. Ali, M. Liu, R. Cava, and N. Ong, *Nat. Mater.* **14**, 280 (2015).
- [11] L. P. He, X. C. Hong, J. K. Dong, J. Pan, Z. Zhang, J. Zhang, and S. Y. Li, *Phys. Rev. Lett.* **113**, 246402 (2014).
- [12] X. Wang, X. Pan, M. Gao, J. Yu, J. Jiang, J. Zhang, H. Zuo, M. Zhang, Z. Wei, W. Niu *et al.*, *Adv. Electron. Mater.* **2**, 1600228 (2016).
- [13] Z. Zhu, B. Fauqué, K. Behnia, and Y. Fuseya, *J. Phys.: Condens. Matter* **30**, 313001 (2018).
- [14] Z. Zhu, J. Wang, H. Zuo, B. Fauqué, R. D. McDonald, Y. Fuseya, and K. Behnia, *Nat. Commun.* **8**, 15297 (2017).

- [15] E. Mun, H. Ko, G. J. Miller, G. D. Samolyuk, S. L. Bud'ko, and P. C. Canfield, *Phys. Rev. B* **85**, 035135 (2012).
- [16] N. H. Jo, Y. Wu, L.-L. Wang, P. P. Orth, S. S. Downing, S. Manni, D. Mou, D. D. Johnson, A. Kaminski, S. L. Bud'ko *et al.*, *Phys. Rev. B* **96**, 165145 (2017).
- [17] X. Xing, C. Xu, N. Zhou, B. Li, J. Zhang, Z. Shi, and X. Xu, *Appl. Phys. Lett.* **109**, 122403 (2016).
- [18] M. Vergniory, L. Elcoro, C. Felser, B. Bernevig, and Z. Wang, *Nature (London)* **566**, 480 (2019).
- [19] F. Tang, H. C. Po, A. Vishwanath, and X. Wan, *Nature (London)* **566**, 486 (2019).
- [20] A. J. Murphy, *J. Inst. Met.* **35**, 107 (1926).
- [21] N. Lee, V. Tan, and K. Lim, *Appl. Phys. Lett.* **89**, 141908 (2006).
- [22] N. Oehl, M. Knipper, J. Parisi, T. Plaggenborg, and J. Kolny-Olesiak, *J. Phys. Chem. C* **119**, 14450 (2015).
- [23] O. Nial, A. Almin, and A. Westgren, *Z. Phys. Chem. Abt. B* **14**, 81 (1931).
- [24] M. Ellner and E. J. Mittemeijer, *Z. Kristallogr.* **218**, 675 (2003).
- [25] C. Fairhurst and J. Cohen, *Acta Cryst. B* **28**, 371 (1972).
- [26] N. Torazawa, S. Arai, Y. Takase, K. Sasaki, and H. Saka, *Mater. Trans.* **44**, 1438 (2003).
- [27] S. Kumar and J. Jung, *Mater. Sci. Eng. B* **178**, 10 (2013).
- [28] Y. Tian, Q. M. Zhang, and Z. Q. Li, *Solid State Commun.* **151**, 1496 (2011).
- [29] See Supplemental Material at <http://link.aps.org/supplemental/10.1103/PhysRevB.101.245102> for the magnetoresistance at different temperatures, the scaling behavior of angular-dependent magnetoresistance, the x-ray diffraction at different temperatures, parameters derived from the LK formula fitting, the polar plot of field angle-resolved resistivity, the magnetization and Hall effect, the fitting of field angle-resolved magnetoresistance, and the field-dependent resistivity  $\rho_{xx}$ ,  $\rho_{yy}$ ,  $\rho_{xy}$ , and conductivity  $\sigma_{xx}$ .
- [30] Q. Niu, W. Yu, K. Yip, Z. Lim, H. Kotegawa, E. Matsuoka, H. Sugawara, H. Tou, Y. Yanase, and S. K. Goh, *Nat. Commun.* **8**, 15358 (2017).
- [31] Q.-H. Yu, Y.-Y. Wang, R. Lou, P.-J. Guo, S. Xu, K. Liu, S. Wang, and T.-L. Xia, *Europhys. Lett.* **119**, 17002 (2017).
- [32] H. Murakawa, M. Bahramy, M. Tokunaga, Y. Kohama, C. Bell, Y. Kaneko, N. Nagaosa, H. Hwang, and Y. Tokura, *Science* **342**, 1490 (2013).
- [33] F.-X. Xiang, X.-L. Wang, M. Veldhorst, S.-X. Dou, and M. S. Fuhrer, *Phys. Rev. B* **92**, 035123 (2015).
- [34] L. He, F. Xiu, X. Yu, M. Teague, W. Jiang, Y. Fan, X. Kou, M. Lang, Y. Wang, G. Huang *et al.*, *Nano Lett.* **12**, 1486 (2012).
- [35] X. Luo, F. Chen, Q. Pei, J. Gao, J. Yan, W. Lu, P. Tong, Y. Han, W. Song, and Y. Sun, *Appl. Phys. Lett.* **110**, 092401 (2017).
- [36] V. P. Jovanović, L. Fruchter, Z. Z. Li, and H. Raffy, *Phys. Rev. B* **81**, 134520 (2010).
- [37] T. Wu, C. Wang, G. Wu, D. Fang, J. Luo, G. Liu, and X. Chen, *J. Phys.: Condens. Matter* **20**, 275226 (2008).
- [38] W. Yu, J. S. Higgins, P. Bach, and R. L. Greene, *Phys. Rev. B* **76**, 020503(R) (2007).
- [39] P. Fournier, M.-E. Gosselin, S. Savard, J. Renaud, I. Hetel, P. Richard, and G. Riou, *Phys. Rev. B* **69**, 220501(R) (2004).